Earth and Planetary Science Letters 513 (2019) 69–80

Contents lists available at ScienceDirect

Earth and Planetary Science Letters

www.elsevier.com/locate/epsl

The electrification of volcanic jets and controlling parameters: A laboratory study

Damien Gaudin *, Corrado Cimarelli *

Ludwig-Maximilians-Universität München (LMU), Department of Earth & Environmental Sciences, Theresienstr. 41, 80333 Munich, Germany

ARTICLE INFO

Article history:
Received 16 November 2018
Received in revised form 14 February 2019
Accepted 17 February 2019
Available online xxxx
Editor: T.A. Mather

Keywords:
plume electrification
lightning
explosive volcanism
volcano monitoring
volcanic jets
Faraday cage

ABSTRACT

Lightning is ubiquitous in large ash-rich eruptions. However, the quantification of the link between volcanic and electrical activities is still missing, hindering its potential for monitoring explosive eruptions. Here, we focus on vent lightning, i.e. discharges occurring within the ash-laden jet. We use a shock tube apparatus generating jets with variable mass of ash, grain size distribution and initial overpressure. The experimental jet is directed inside a Faraday cage, where the current (flux of electrical charges) is measured, allowing to estimate the total charge of the plume, and the number and magnitude of jet-to-ground discharges. Three mechanisms control the electrical structure of the jet: (i) the tribocharging of the ash particles against the shock tube walls; (ii) the particle–particle tribocharging in the jet flow; (iii) the particle and charge separation according to the particle size, leading to the formation of clusters of electrical charges. The number and magnitude of discharges mainly rely on the two latter mechanisms: while the particle–particle interactions define the total charge in all the clusters, which is linked to the observed cumulative magnitude of the discharges, the jet structure defines the size of the individual clusters, and, in turn, how the cumulative magnitude is partitioned on a number of discharges. Finally, our experimental relationships between eruptive and electrical parameters are compatible with field observations, suggesting that the pattern of discharges recorded by electrical monitoring systems can be used to interpret the structure of volcanic jets and their dynamic evolution.

1. Introduction

Ash electrification is a common feature in ash-rich volcanic plumes (McNutt and Williams, 2010). It may produce volcanic lightning at different stages of the plume development: (i) during the jet phase, when the plume motion is driven by inertia (vent discharges according to Thomas et al., 2010 classification) (ii) during the buoyant rise of the plume (near vent discharges) or (iii) within the umbrella of the plume (plume lightning).

The emission of radio-frequency impulses by electrical discharges makes them easily detectable by instrumental networks with different detection ranges. Local Lightning Monitoring Arrays (LMA) (Behnke and McNutt, 2014; Thomas et al., 2007, 2004) or global antenna networks such as the World Wide Lightning Location Network (WWLLN) and the ATDnet system (Bennett et al., 2010; Van Eaton et al., 2016, 2017), enable instrumental detection of volcanic explosive eruptions at safe distance and in all weather conditions (Behnke and McNutt, 2014). Several studies of recent eruptions have highlighted the link between electrical activity and the spatial and temporal evolution of volcanic plumes (Aizawa et al., 2016; Behnke et al., 2013; Thomas et al., 2010). Indeed, eruptions such as Augustine (2006) (Thomas et al., 2007, 2010, Redoubt (2009) (Behnke et al., 2013), Eyjafjallajökull (2010) (Arason et al., 2011; Bennet et al., 2010; Méndez Harper and Dufek, 2016), and more recently Bogoslof (2017–2018) were monitored from an electrical point of view. Meanwhile, the frequent eruptions of Sakurajima (Japan) have led to numerous studies using local arrays trying to link volcanic processes and electrification (Miura et al., 2002; Cimarelli et al., 2016).

So far, no model exists to link the dynamics and the electrical activity of a volcanic plume, thus hindering the derivation of quantitative real-time information on the eruption from instrumental detection of electrical signal. Field studies have suggested that, although magma composition seems to have no effect (McNutt and Williams, 2010), the electrical activity may correlate with the magnitude of the eruptions.

* Corresponding authors.
E-mail addresses: damien.gaudin@min.uni-muenchen.de (D. Gaudin), cimarelli@min.uni-muenchen.de (C. Cimarelli).

https://doi.org/10.1016/j.epsl.2019.02.024

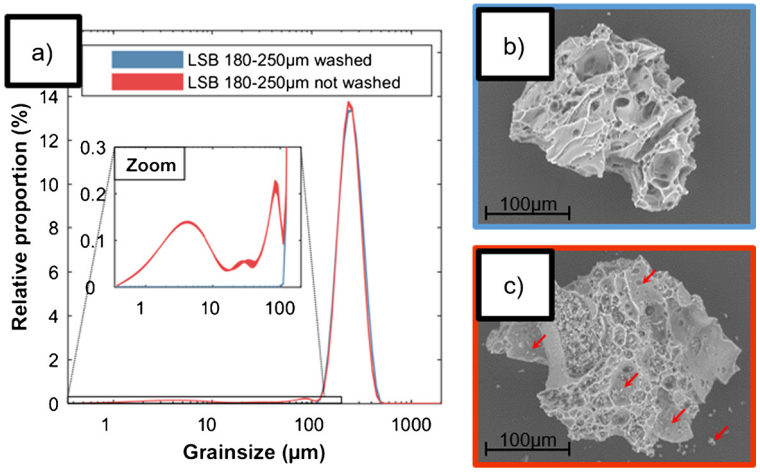

Fig. 1. a) Grain-size distribution of the sample before and after the washing procedure. Particles below 63 µm (fine particles) represents 3.96% of the volume in the non-washed sample and are below detection limit in the washed sample. b) and c) SEM close-up of washed (b) and non-washed particles (c): fine particles (some of them being marked by red arrows) are aggregated on the bigger ones only for the non-washed sample (some of them detached during the sample preparation). (For interpretation of the colors in the figure(s), the reader is referred to the web version of this article.)

From an experimental point of view, studies have been focusing on the charging mechanism of solid particles, especially aiming at disentangling the effects of tribo-electrification (exchange of electrical charges between two bodies rubbed together, see Harrison et al., 2010; Houghton et al., 2013; Méndez Harper and Dufek, 2016) from those of fracto-electrification (caused by the fragmentation of the erupting magma and pyroclasts, see James et al., 2000, 2008; Méndez Harper et al., 2015). However, these experiments only focus on the charging mechanism of volcanic particles and neglect the equally important mechanisms of discharge. In addition, they do not provide scalable numbers to transpose the results in the context of volcanic explosive eruptions. Finally, they mainly focus on the near-vent and plume lightning, neglecting the specificities of vent lightning which is the earliest detectable electrical signal and is thus crucial for real-time monitoring.

Focusing on the jet phase and vent lightning, Cimarelli et al. (2013) managed to produce electric discharges by rapidly decompressing a dry gas-particle mixtures in a shock tube apparatus. Their experiments succeed in reproducing the whole charge-discharge process, from the electrification of the particles, through the particle and charge separation, to the generation of the discharges. Electrical discharges were observed both visually using high-speed video recordings and through variations of the electrical potential using small antennas.

In this study, we further implement the experimental setup described by Cimarelli et al. (2013) and setup a data processing method in order to more precisely quantify the charging of the particles and the discharges within the jet (referred as "vent lightning" in Thomas et al., 2010). By using a Faraday cage, we compute the net electric charge associated with the gas-particle flow, and the number and magnitude of the electrical discharges generated within. We focus our analysis on the effect of three main parameters, recognized to be crucial for the generation of volcanic lightning: (i) the mass of ejected particles (eruption magnitude), (ii) the pressure within the conduit and in the jet flow (eruption intensity) and (iii) the proportion of fine particles over the total solid load in the flow (grainsize distribution). Others factors that may play a significant role on electrification, (such as atmospheric conditions, water content, ash composition and crystallinity or temperature) have been deliberately excluded from the analysis for simplicity; however, the method developed here will be easily applicable to explore the effects of these parameters.

2. Experimental procedure

2.1. Sample preparation

We use natural volcanic ash particles to run the experiments. To assure reproducibility of the experiments, we use ash from the lower unit of the 13 ka Laacher See eruption (East Eifel volcanic field, Germany), which is quarried in large quantities for industrial purposes, and sieved between 90–300 µm by ROTEC GmbH (Mueller et al., 2017). The ash is phonolitic in composition (SiO_2 ~55 wt%; Al_2O_3 ~20.5 wt% NaO ~11 wt%; K_2O ~5.5 wt%) and contains 5–8 wt% of phenocrystals, in particular sanidine, plagioclase and clinopyroxenes (Wörner and Schmincke, 1984). Particles have a mean density of 1383 g/m^3 (Douillet et al., 2014). To guarantee a replicatable grainsize distribution, we further sieve the ash during 15 min to select grains between 180 and 250 µm. The grainsize distribution of the sample is determined by a laser particle size analyzer (LPSA; model Coulter LS230). The LPSA shows that the sieved sample still contains ~4 vol% of fine ash (i.e. grainsize <63 µm, Fig. 1a). Scanning electron microscope (SEM) images show that the fine ash is in fact aggregated on larger particles (Fig. 1c) after the sieving. We use a water jet to wash the sieved samples in order to detach the fine ash and further reduce the grain size distribution of the samples. Ash was then dried during 12 hr in an oven at 95 °C, and stored in room conditions to ensure the same humidity as the non-washed samples. Both LPSA measurements (Fig. 1a) and SEM imaging (Fig. 1b) demonstrate that, after washing, the amount of fine ash sticking to larger particles is below detection limit. By blending the washed and non-washed samples, we are thus able to tune the amount of fine ash between 0 and 4% in the experimental runs.

2.2. Experimental apparatus

The experimental apparatus (Fig. 2) is a modified version of the shock tube apparatus first described in Alidibirov and Dingwell (1996) and further improvements (e.g. Alatorre-Ibargüengoitia et al., 2010; Kueppers et al., 2006). The sample is inserted in shock tubes with variable diameter of 20, 26 or 33 mm. We prevent the compaction of the sample by avoiding shaking or knocking the autoclave. The shock tube is sealed by an imprinted diaphragm of copper or iron ("Lower diagram" in Fig. 2). The maximum pressure that the diaphragm can hold is empirically determined and depends on the material used, the thickness of the diaphragm, and

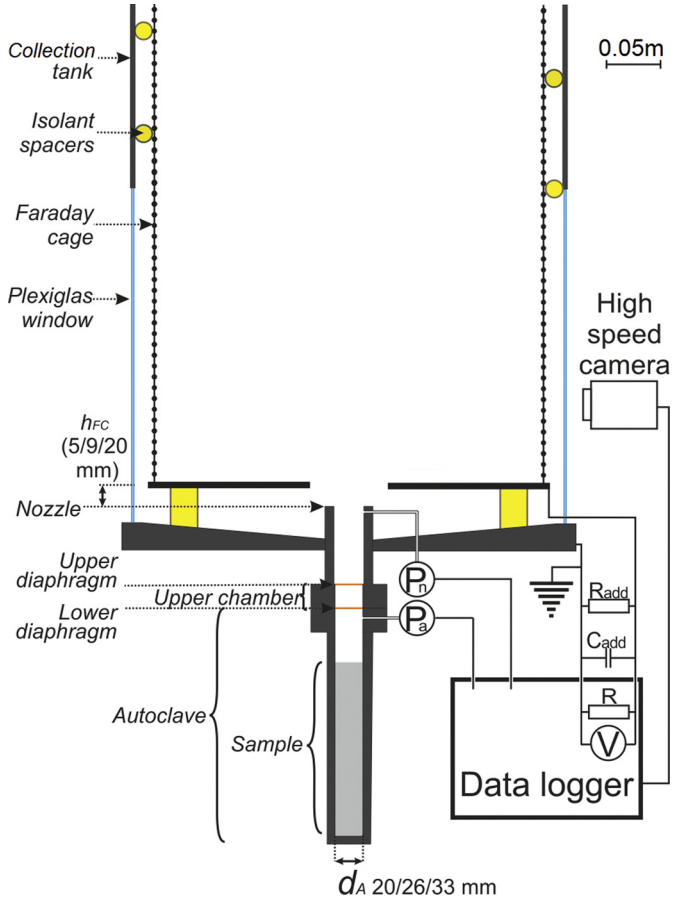

Fig. 2. Experimental setup. Plastic spacers (in yellow) insulate the Faraday cage from the autoclave and the collection tank. d_A and h_{FC} represents respectively the diameter of the autoclave and the vertical spacing between the Faraday cage and the nozzle, that can be tuned.

the depth of the imprint. The pressure in the autoclave is increased by progressively introducing argon gas, until the diaphragm fails. To exactly control the bursting pressure of the diaphragm, a second diaphragm can be placed on top, delimiting a small upper gas chamber. In this configuration, the two diaphragms are typically chosen to hold 75% of the target pressure and the pressure in the upper chamber is set to be approximatively 50% of the target pressure in the autoclave. In this way, the pressure in the shock tube can be precisely tuned and the explosion is triggered by suddenly increasing the pressure in the upper chamber only. The rupture of the upper diaphragm precipitates the instantaneous rupture of the lower diaphragm inducing fast decompression of the gas-particle mixture, which expands in the collection tank above generating a jet flow.

To monitor the jet dynamics, we used a static pressure sensor at the top of the autoclave and a dynamic pressure sensor at the nozzle (respectively P_a and P_n in Fig. 2). In parallel, some experiments were filmed using a V711-Phantom high-speed camera (typically 400×400 pixels definition at 40 000 fps).

The gas/particle mixture is ejected in a 4 m-high 0.4 m-diameter cylindrical tank at room pressure and temperature. Inside the tank, a 2 m-high 0.36 m-diameter Faraday cage (metallic mesh with 1 cm spacing) is installed. The bottom part of the Faraday cage consists of a metal plate with a 7 cm hole in the middle which hosts the autoclave nozzle. The vertical spacing between the bottom of the Faraday cage and the nozzle (h_{FC}, see Fig. 2) can be adjusted according to the jet characteristics and the number and size of sensors fitting in this space. The Faraday cage is insulated from the walls and bottom of the tank by insulating plastic spacers. Generally, the mesh grid in a Faraday cage should be smaller than the wavelength of the recorded signal (Thirumal Murugan et al., 2015). Consequently, our cage would allow recording signals lasting at least 0.035 µs.

The autoclave is electrically grounded. In contrast, we set a resistor between the Faraday cage and the ground. The measurement of the voltage (V) across the resistor allows to compute the electric current I (i.e. the time derivative of the charges Q) from the ground to the Faraday cage, following Ohm's law:

$$\frac{dQ}{dt} = I = \frac{V}{R_{tot}} \tag{1}$$

where R_{tot} is the total resistance of the circuit. In our case, R_{tot} is given by the sum of the internal resistance of the datalogger R_{DL} (Yokogawa WE7000) and the resistance of an additional resistor R_{add}, which we use together with an extra capacitor C_{add} to decrease the amplitude of the signal and avoid saturation. The total resistance of the circuit is then:

$$\frac{1}{R_{tot}} = \frac{1}{R_{DL}} + \frac{1}{R_{add}} \tag{2}$$

To allow comparison between different experiments, we define the beginning of the burst as coincident with the beginning of the pressure drop in the shock tube (i.e., $t_0 = 0$ when the pressure inside the autoclave drops below 90% of the initial pressure). Note that the pressure sensor is located at the top of the autoclave, but at the end of a 150 mm capillary tube, thus causing a short time delay between the diaphragm rupture and the recorded decrease of pressure.

Although we will limit our study on the three relevant parameters for ash electrification and volcano monitoring, the setup is very flexible and could be easily tuned to explore the effect of additional parameters such as ash and atmospheric temperature, water content, ash composition and crystallinity.

2.3. Data processing

The electrical current I measured by the data logger (referred hereafter as raw signal) is made of the superimposition of two signals, each of them reflecting a distinct mechanism of charge transfer: (i) a slowly fluctuating baseline (hundreds of µs timescale) representative of a constant current (i.e. flow of charge) entering the Faraday cage, and (ii) sudden rises followed by exponential decays. By comparing electrical signal and high-speed video recording of the experiment, Cimarelli et al. (2013) demonstrated that the sudden rise in the electrical current is coincident with the flashes from the jet to the ground. The exponential decay corresponds to the impulse response of the circuit (*IRF*), reflecting the time needed for the Faraday cage to equilibrate its charges with the ground. The intracloud discharges do not provoke a charge transfer from the Faraday cage interior to the ground, hence they are not detectable with our setup.

The main goal of the data processing is to separate the two signals. In that scope, we first remove the effect of *IRF*. The *IRF* is an exponential function, whose characteristic time is equal to $R_{tot}C_{tot}$, where R_{tot} and C_{tot} are the total resistance and capacitance of the circuit. The total capacitance (C_{tot}) of the circuit is the sum of the capacitance of the capacitor (C_{add}) and the capacitance of the Faraday cage itself (C) put in parallel. Hence, to get the capacitance of the Faraday cage, we need to use the signals produced by some isolated flashes, and fit the evolution of the electric current using the equation:

$$\begin{cases} I = I_{\text{offset}} & \text{for } t < t_{\text{flash}} \\ I = I_{\text{offset}} + I_{max}\exp(-\frac{t-t_{\text{flash}}}{R_{tot}C_{tot}}) & \text{for } t \geq t_{\text{flash}} \end{cases} \tag{3}$$

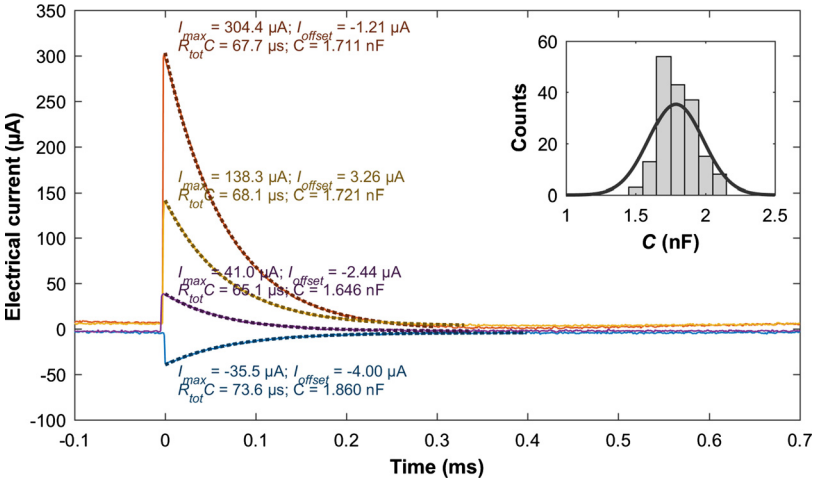

Fig. 3. Determination of the capacitance of the Faraday cage. Four examples of flashes are represented and fitted using equation (3), providing each an estimate of the capacitance of the Faraday cage (in these cases, $C_{add} = 0$ nF and $R_{tot} = 39\,562\ \Omega$). The inset represents the histogram of the capacitances from 175 flashes, providing an estimate of the capacitance of the Faraday cage of 1.79 ± 0.03 nF (95% confidence interval error).

The fit of 175 flash events provides a value of 1.79 ± 0.03 nF for the capacitance of the Faraday cage (Fig. 3).

The IRF of the datalogger is thus (note that the time integration of the IRF equals 1):

$$\begin{cases} IRF = 0 & \text{for } t < 0 \\ IRF = R_{tot}C_{tot}\exp(-\frac{t}{R_{tot}C_{tot}}) & \text{for } t \geq 0 \end{cases} \quad (4)$$

Since the raw signal is the convolution of the current with the *IRF*, the current is the deconvolution of the raw signal by the *IRF*. This deconvolution process is achieved using Matlab.

The deconvoluted signal is the superimposition of a slowly fluctuating baseline (hundreds of µs timescale) and some Dirac deltas, corresponding to the discharges. To distinguish the two components, we use the following procedure: (i) the peaks are removed from the deconvoluted signal by applying a median filter so that the obtained signal corresponds to the baseline; (ii) the baseline signal is subtracted from the deconvoluted signal so that the residual is a signal centered on zero and displaying the peaks; (iii) a threshold is applied to distinguish the peaks from the noise. In order to define this threshold, we apply this procedure on the signal recorded before starting the experiment, thus computing the standard deviation of the noise. We set the threshold at a minimum of 6 times the standard deviation so that the number of false-positives in 1,000,000 data points experiments is lower than 1‰. Peaks detected on consecutive data points are considered to belong to a single event, and are merged by summing up their intensities. This procedure allows us to make a database of the flashes observed, each of them being associated to a timing after the beginning of the explosion and a magnitude (i.e. amount of charge transferred). The total magnitude of the discharges for each experiment is computed by summing up all the individual magnitudes of discharges.

The time-integration of the electrical current recorded by the data logger allows to estimate the net charge inside the Faraday cage:

$$Q(t) = \int_0^t Idt \quad (5)$$

Note that, since the *IRF* is normalized (equation (4)), the integration can be achieved indifferently on the raw or the deconvoluted signal. This allows also to remove directly the effect of discharges from the current measured to obtain only the net charge associated with the jet entering the Faraday cage.

3. Results

3.1. Characteristics of electrical activity

We conducted a total of 46 experiments. Detailed results for all experiments, automatically generated by a processing code, are available as supplemental material at GFZ portal (Gaudin and Cimarelli, 2019). Out of this total, 17 "blank experiments" were conducted with no ash, which allow us to distinguish the effect of the gas from those of the ash.

Fig. 4 shows the results for two typical experiments, one with ash (EXP119) and one "blank" (EXP114). The time $t = 0$ of the experiment is arbitrarily set when the pressure measured in the autoclave drops below 90% of the initial pressure (Fig. 4a). The dynamic pressure (Fig. 4b) increases quasi-instantaneously when the gas (no particles yet) escapes the nozzle. In the case of ash experiments, the pressure further increases while the particles are expelled until the maximum recorded pressure (typically 1/10 to 1/15 of the initial pressure within the autoclave) when also the particles are ejected in the flow. Finally, in both cases, the dynamic pressure decreases quasi exponentially.

In the presence of ash, the current from the Faraday cage signal displays a superimposition of peaks followed exponential decays on a slowly fluctuating baseline (Fig. 4c). The exponential decays represent the instrumental response of the circuit to the impulsive signal associated to the discharge events, while the baseline (i.e. the background signal) is indicative of the flux of charges associated with the flow of gas and particles together. From a chronological point of view, all experiments follow a similar pattern. The ejection of the gas is associated to a negative current (-7.5 µA at $t = -0.5$ s and -3.5 µA at $t = -0.4$ µs for EXP114 and EXP 119, respectively). An additional negative signal may be visible before in the experiments with two diaphragms, corresponding to the ejection of the gas between the two diaphragms. Positive discharges (i.e. neutralizing negative charges) are visible in presence of ash after $+0.5$ ms and last until $+2.2$ ms. This timing corresponds to the ejection of the first particles. About 15 large discharges (corresponding to flashes in the video) are clearly visible, in association with some smaller discharges (Fig. 4f). Although the magnitude of the discharges remains constant, their rate slightly decreases with time. After $+3$ ms in Fig. 4, and in some cases up to $+250$ ms, late discharges can be still recorded. Unlike the early ones, late discharges (i) are of both polarities, (ii) also occur in blank experiments charged with gas only (e.g. EXP120 in Gaudin and Cimarelli, 2019), and (iii) tend to disappear after thorough cleaning of the

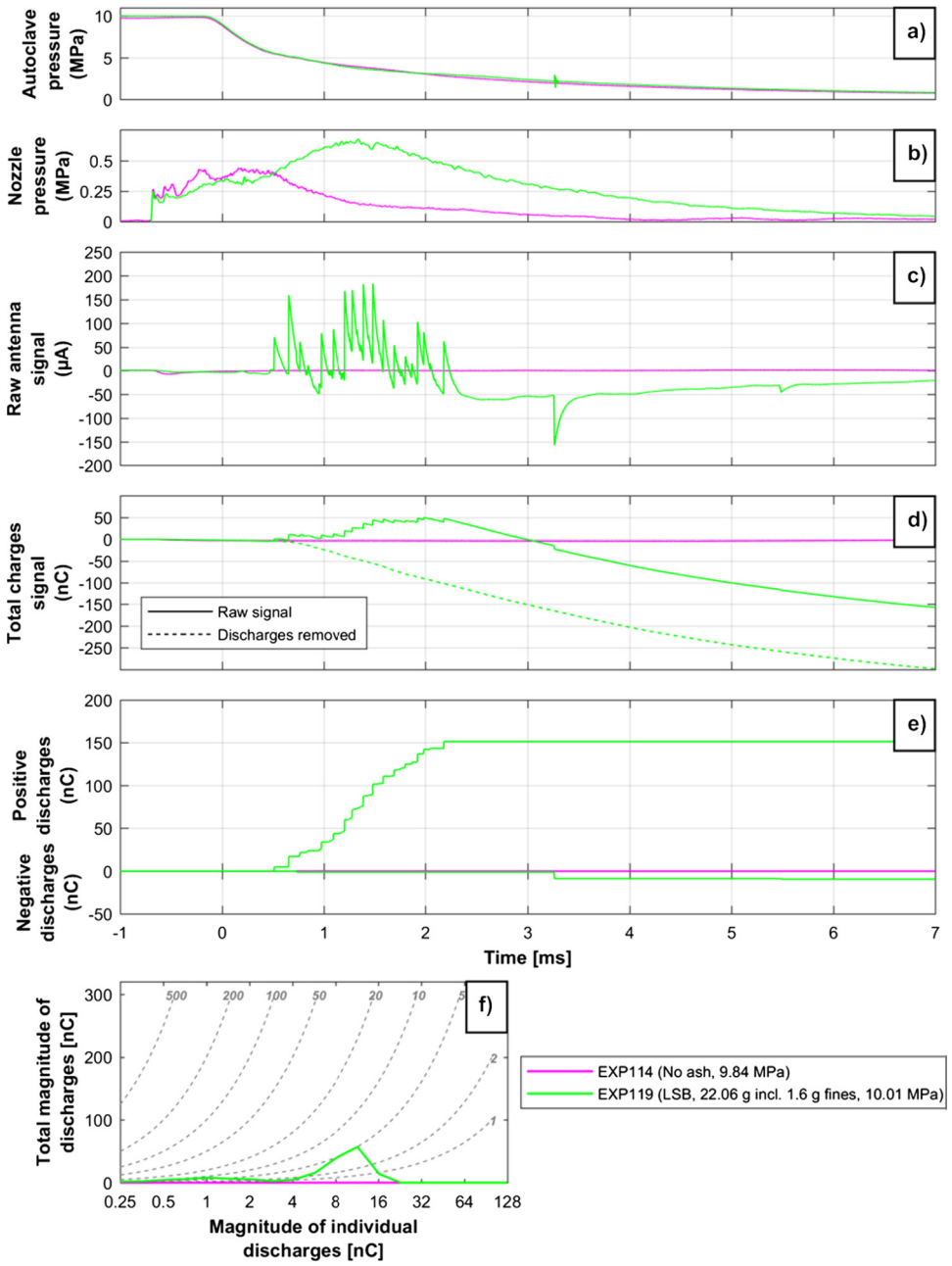

Fig. 4. Example of signals from a typical experiment (EXP 119, in green) and a blank one (EXP 114, in magenta): a) static pressure at the top of the shock tube; b) dynamic pressure at the nozzle; c) Faraday cage current (I) measured from the Faraday cage to ground (see equation (1)); d) total charge in the Faraday cage (plain lines, equation (5)) and comparison with the charge that would be inside the cage if no discharges were occurring (discharges were removed using the procedure described in section 2.3). In EXP 114, no discharges are detected, hence the two lines remain superimposed; e) total magnitude of the positive and negative discharges; f) binned distribution of discharge magnitude for the sets of (each bin represents $0.5\log_2$-units). The dashed lines show the number of discharges of a given magnitude. (See description in the text.)

setup. We interpret them as the effect of residual ash from previous experiments stuck on the apparatus (in particular on the mesh of the Faraday cage) that is remobilized by the shock wave or the particle-laden flow itself. These signals are very difficult to avoid, even after very careful cleaning of the apparatus. In addition, we note that they are associated to perturbations in the dynamic pressure sensor signal. For these reasons we will not take them into consideration for the rest of the study and focus our analysis to the first 7 ms of each experiment. This time window is long enough to observe the evolution of the gas-particle jets until it reaches quasi steady-state conditions and before the expanding flow starts interfering with the Faraday cage and the tank.

The variation in the net charge inside the tank, i.e. the time integration of the raw signal (equation (5)) is represented in Fig. 4d (solid line). This signal has two components: the net charge carried by the particles entering the Faraday cage and the discharges. By removing the effect of the discharges using the procedure described in section 2.3, we determine the net charge of the particles to be negative (Fig. 4d, dashed line). In presence of ash, the negative charges are periodically neutralized by positive discharges and, up to +3 ms, the net charge inside the autoclave is positive. Here, we highlight that positive discharges (i.e. discharges neutralizing negative charges) are observed in a dominantly negatively charged flow. When the discharges cease, the flux of negative charges brings the net charge inside the Faraday cage to negative values again. In most of the experiments (e.g. EXP138 in Fig. 6), the net polarity of the flow becomes positive after a variable time (6–20 ms); however, at this time, the jet may start interacting with

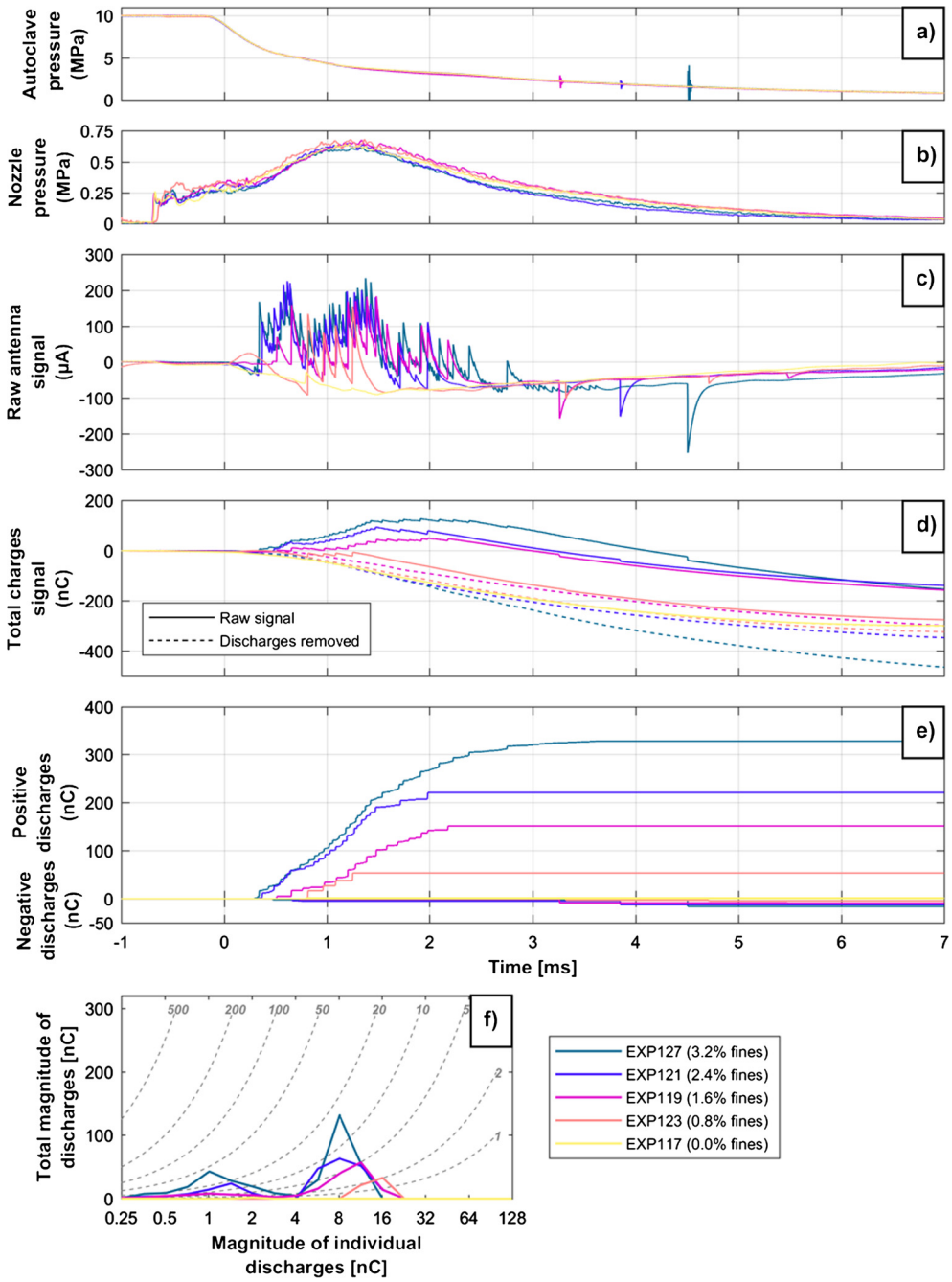

Fig. 5. Results of 5 experiments showing the effect of the proportion of fine particles on the electrical signal. Experiments were made at an initial autoclave pressure of 10 MPa with 22 g of ash (same panels as in Fig. 4).

the Faraday cage itself and the expansion tank, thus making it of more difficult interpretation.

Fig. 4e represents the total amount of charges neutralized by instantaneous discharges of opposite polarity. All the discharges in the first 3 ms of EXP119 are positive, hence they neutralize negative charges inside the Faraday cage. The curve displays an initial linear increase (i.e. constant rate of discharges) before progressively reaching a plateau after 3–4 ms.

3.2. Factors enhancing or inhibiting the electrical activity

3.2.1. Influence of grainsize distribution

In our experiments, we use a bimodal grainsize distribution: by mixing washed sample with non-washed samples (see section 2.1), we can control the mass proportion of fine particles (i.e. particles below 63 μm) from 0 to 4% (Fig. 5). The variation of pressure inside the autoclave (Fig. 5a) or at the nozzle exit (Fig. 5b) shows that the dynamics of the jet do not change significantly with increasing proportion of fines.

Fig. 5c shows that, in absence of fine particles, no relevant discharges are observed and the electrical current is negative. Increasing the amount of fine ash, the number of discharges also increases, as well as the time window during which the discharge transients are observed (Fig. 5f). Conversely, the overall magnitude of the discharges seems to be similar in experiments with variable amounts of fines (Fig. 5c, 5e and 5f). Overall, the total magnitude of the discharges is proportional to the initial amount of fine ash in the sample (Fig. 5e). Conversely, removing the effect of the discharge transients, the net charge inside the Faraday cage shows no real dependence on the total amount of fine particles (Fig. 5d).

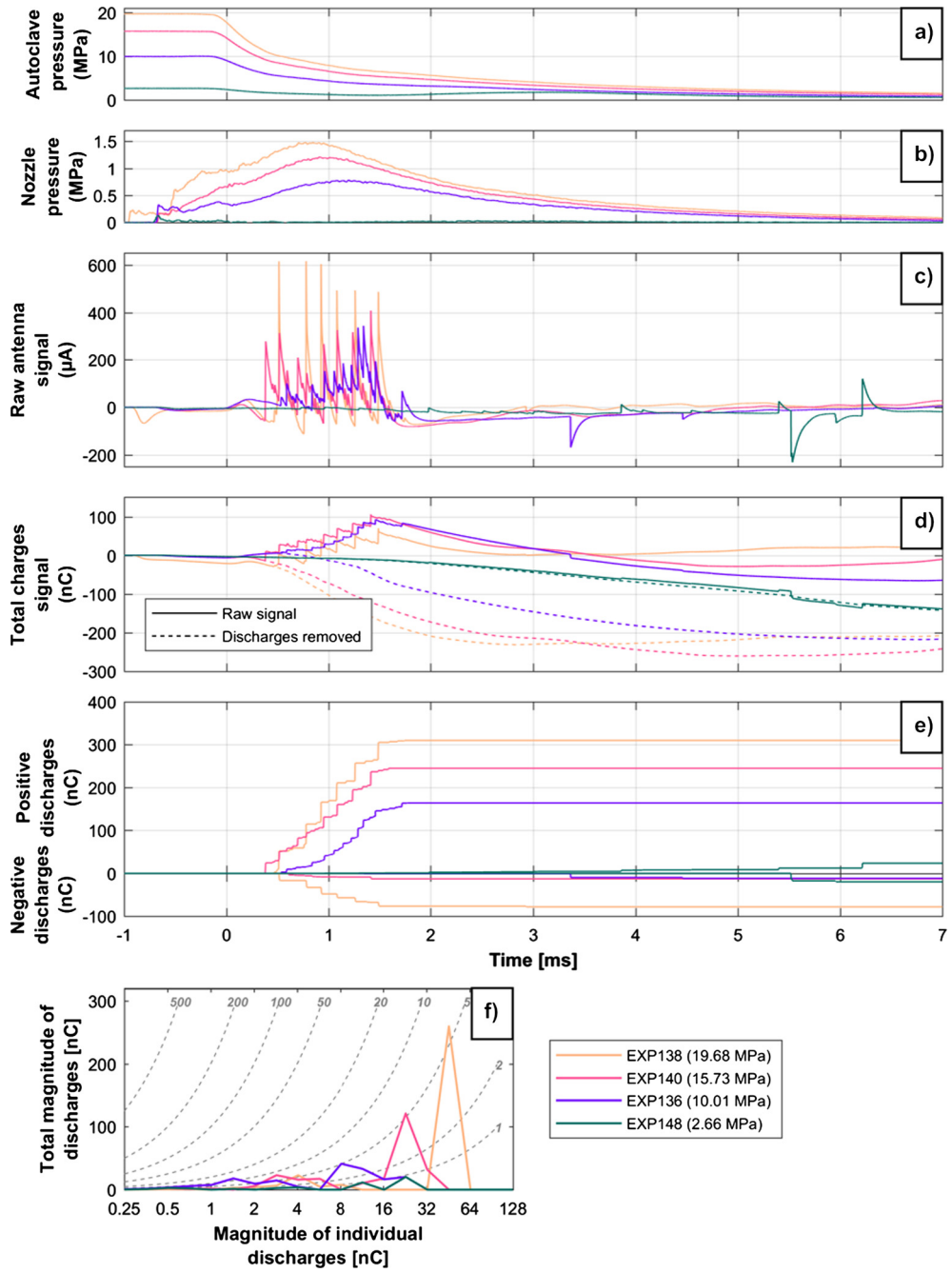

Fig. 6. Results of 4 experiments showing the effect of the initial autoclave pressure on the electrical signal. Experiments were made with 22 g of ash including 2.4% of fine particles (same panels as in Fig. 4).

3.2.2. *Influence of initial pressure*

By changing type of diaphragms, the initial pressure inside the autoclave can be varied from 2 to 20 MPa. Increasing the autoclave pressure increases the observed pressure at the nozzle accordingly (Fig. 6b). Unlike the proportion of fines, increasing the starting pressure also increases the magnitude of the largest discharges without changing their number nor the time window during which they occur (Fig. 6c and Fig. 6f). Before the jet starts interacting with the Faraday cage (around +3 ms), a linear relationship between the initial pressure and the charge entering the Faraday cage can be observed (Fig. 6d). Overall, it can be found that the total magnitude of the discharges is proportional to the initial pressure (Fig. 6e).

3.2.3. *Influence of mass*

The last forcing parameter we vary in the experiments is the initial mass of ash inside the autoclave. Because the evolution of the pressure as well as the velocity of the particles depends mainly on the length of the autoclave (Alatorre-Ibargüengoitia et al., 2011, 2010), we used autoclaves of different diameters (20, 26 and 33 mm) to account for the mass. Concerning the charges and the discharges within the Faraday cage, the effect of the mass is very similar to the effect of the initial pressure in the autoclave. Firstly, the magnitude of the discharges increases linearly with the increasing mass of the sample but the number of discharges remains constant (Fig. 7c and Fig. 7f). Secondly, the net charge entering the Faraday cage grows linearly with the increasing mass (Fig. 7d). The

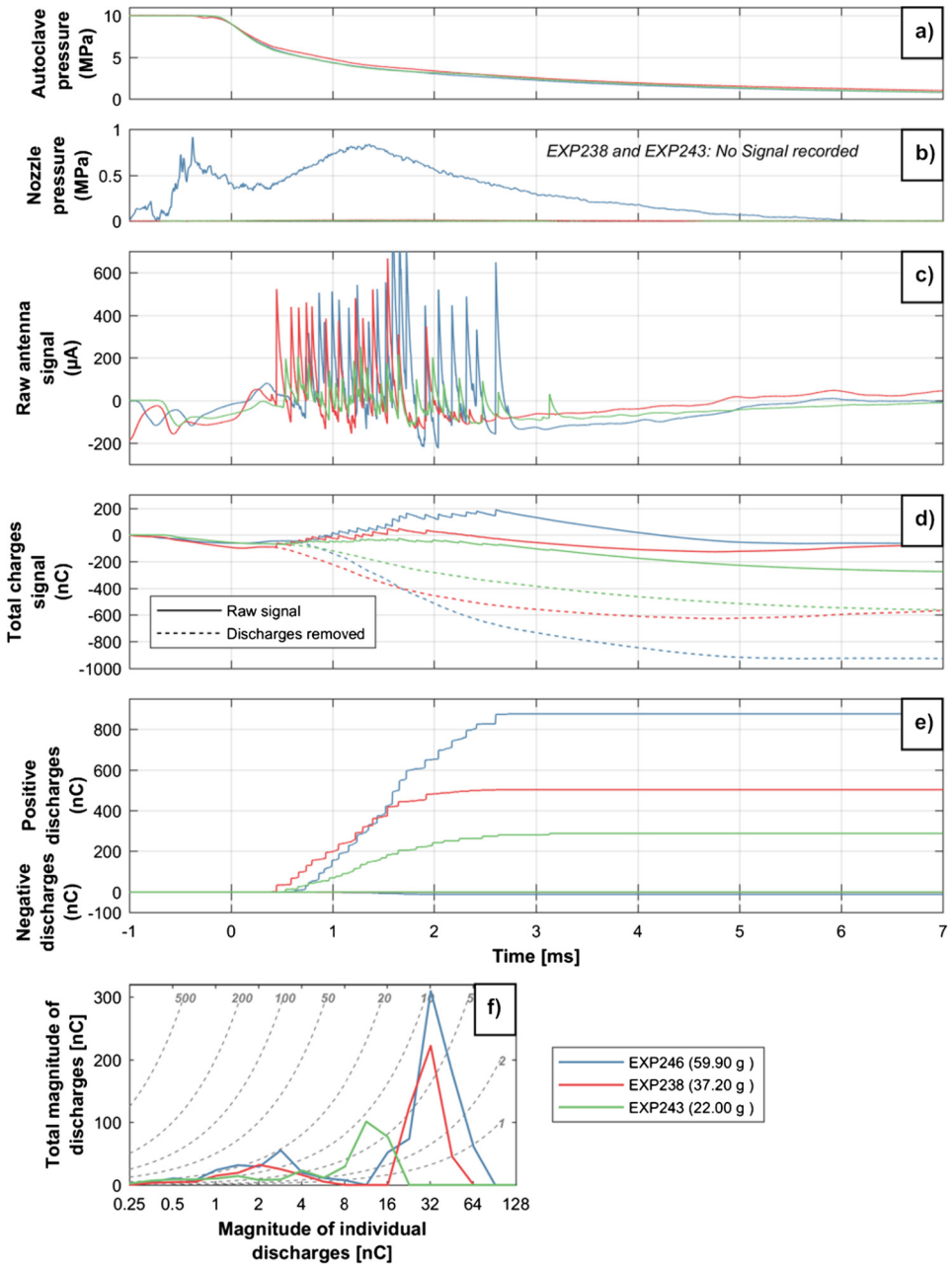

Fig. 7. Results of 3 experiments showing the effect of the mass of sample on the electrical signal. Experiments were made with an initial autoclave pressure of 10 MPa with 2.4% of fine particles (same panels as in Fig. 4).

same proportionality is observed for the number of positive discharges (Fig. 7e).

4. Discussion

4.1. Experiment analysis

4.1.1. Particle charging

In all the experiments, the evolution of the charging inside the Faraday cage follows a similar pattern. The gas itself is negatively charged, as evidenced by the signal produced by blank experiments (no particles loaded in the autoclave) and in all the other experiments by the expanding gas escaping from the upper diaphragm chamber. In these cases, the expanding argon typically carries a charge of −10 to −50 nC. However, the magnitude of the net charge of the particle-laden jet is at least 10 times higher, typically between −100 and −900 nC. The negative charging of ash particles is in good agreement with the electrostatic theory (Lacks and Levandovsky, 2007) predicting that the negative charge should flow from the material with the highest work function (in our case the stainless steel, around 4.5 to 5 eV, see Wilson, 1966; Surplice and D'Arcy, 1972) to the lowest one (in our case, silicates, around 3.25 eV, see Deng et al., 2010).

This evidences that the electrical charges are mainly carried by the solid particles. Results show that the net charge of the particles does not depend on the proportion of fine particles but only on the total mass of the sample and the initial pressure in the autoclave. However, experiment replicates show that the net charge inside the Faraday cage does not reach a plateau over the full duration of the experiments (Figs. 4–7 panels d). This is very likely due to the particles escaping through the mesh of the Faraday cage (note that the volume of the Faraday cage represents only 90% of the volume of the collection tank), thus preventing the charging to reach a stable maximum value and hindering a fine quantitative analysis of

the dependence of net charge upon total mass and initial pressure in the autoclave.

Two particle charging mechanisms are usually invoked based on field and lab experiments (James et al., 2008; Méndez Harper and Dufek, 2016; Méndez Harper et al., 2018): triboelectrification, i.e. the exchange of charges between two objects rubbing together (particle vs. particle or particle vs. autoclave, in our case, see Alois et al., 2017; Harrison et al., 2010; Houghton et al., 2013; Méndez Harper and Dufek, 2016) and fractoelectrification, i.e. the emission of ions during the brittle fracture of the particles (James et al., 2000, 2008; Méndez Harper et al., 2015). In our experiments, the negative net charging carried by the particle-laden jet entering the Faraday cage implies a charge exchange with the ground. Statistical analysis of Figs. 5–7 (panel d, dashed lines) suggest that the net charge of the plume depends on the mass of ash and the initial pressure of the gas. The correlation between the mass and the net charge could be linked to the fact experiments with more ash have been conducted in autoclaves with a larger diameter, so that more particles could rub against the autoclave and be charged. Similarly, higher pressures might enhance the autoclave-particle interactions, by increasing the number of particles rubbing against the autoclave, or the efficiency of the charging. In this context, the absence of extra-charging for those samples enriched in fine particles would imply that small particles probably do not have enough inertia to impact or rub against the autoclave with sufficient energy once detached from the biggest ones.

Although the Faraday cage allows measuring the total net charge associated with the particle-laden jet, it does not provide information on the charge associated with individual particles. Indeed, a strong heterogeneity in particle charges can be deduced from the results of the experiments. In particular, during the first 3 ms of the experiments (Fig. 4) positive discharges neutralize negative charges, although the total net charge in the tank is positive. This proves the simultaneous presence of positive and negative clusters of charges in the jet, and that particle/particle charging in the flow is more efficient than particle/autoclave charging (if this latter process was predominant, we would expect mainly particle of the same polarity entering the Faraday cage).

Concerning the particle/particle charging mechanism, although ash could experience further fragmentation during the decompression, we can exclude any significant effect in our case. In fact, according to Stokes law, particles of 63 μm would need 24 s to settle from the top of the 4 m high collection tank. Yet, when using washed samples, all the particles are able to settle within this time frame, suggesting that a negligible proportion of fine particles is generated during the flow and that fragmentation is a marginal phenomenon in our experiments. Thus, tribocharging appears here to be the key mechanism for the particle/particle charging. However, other charging mechanisms cannot be excluded *a priori*. Among others, one mechanism of charging could be related to the disaggregation of fine particles from the bigger ones. Indeed, aggregation can be achieved by electrostatic forces (Del Bello et al., 2015; James et al., 2003; Mueller et al., 2017), which might generate a difference of charge upon disaggregation.

4.1.2. Discharges

Discharges are observed during a short time-interval, during the jet phase, only when (i) particles are expelled from the autoclave (as showed by the high-speed videos) and when (ii) the flow at the vent is overpressured (as measured by the dynamic pressure sensor and confirmed by the shape of the expanding jet when exiting the nozzle).

Cimarelli et al. (2013) hypothesized that the separation of particles of different sizes is based on their tendency to be deviated from a straight trajectory. This effect is best described by the Stokes number of the particles, computed as the ratio between the relaxation time τ_f (i.e. the characteristic time of the exponential decay of the velocity due to drag) and a characteristic time of the flow τ_p (usually the vent diameter divided by the jet velocity). For our experiments, using the Ergun (1952) equation for the conditions inside the autoclave, particles of 63 μm in the 26 mm diameter autoclave at 10 MPa (the arbitrary limit between fine and large particles) have a relaxation time of 0.6 ms (Cimarelli et al., 2013), while, using the methodology from Cigala et al. (2017), the relaxation time is 0.17 ms when the gas is fully expanded (0.027 ms and 0.58 ms for small and large particles with average diameters of 10 and 215 μm, respectively). Note that these values (i) are associated with large uncertainties due to the impossibility of measuring the actual velocity of single particles on the high-speed videos (mainly due to image resolution), and (ii) increase with time from the start of an experiment as a consequence of the progressive decrease of pressure and particle exit velocity. However, such values are compatible with the model of Cimarelli et al. (2013), where small particles ($d < 63$ μm and $St \lesssim 1$) tend to follow the turbulence at the edge of the jet while large particles ($d > 63$ μm and $St \gtrsim 1$) have straight trajectories along the core of the jet. This model would also explain the absence of flashes at later stages during the experiments: the absence of overpressure provokes no jet expansion at the exit of the nozzle and all particles follow a straight trajectory, preventing particle separation and electrical cluster formation.

Theoretical (Lacks and Levandovsky, 2007) and experimental (Forward et al., 2009; Lee et al., 2015) studies have shown that, in case of triboelectrification, large particles tend to charge positively while small ones need to charge negatively. In our experiments the observed discharges are positive, and since they occur between the jet and a grounded object (the nozzle or the autoclave, both grounded), they neutralize negative charges in the jet, i.e. charges carried by the small particles. This observation is once again compatible with a scenario in which a small portion of fine particles are entrained in the turbulent shear layer of the jet, and discharged from there. This would also explain the peculiar curved trajectories of the flashes following the margin of the flow, as often observed in our experiments (Fig. 8). It is worthwhile here to remark that, as described in detail by Mendez-Harper et al. (2018), discharges are favored by zones of under-pressurization within the flow. As a matter of fact, according to the Paschen law the electrical breakdown value of the gas phase increases linearly with its pressure. In our case, this lower-pressure zone corresponds to the portion of the jet undergoing Prandl-Mayer expansion (i.e. the overpressurized part of the jet) and is delimited by the barrel shock structure.

Panels e of Figs. 5–7 demonstrate that the total magnitude of discharges is proportional to all three parameters studied. However, panels f of the same figures suggest that they play different roles in the generation of the discharges. In particular, it is interesting to note that the number of discharges is proportional to the fraction of fine particles (Fig. 5f). while their magnitude is linearly linked to the autoclave pressure and the sample mass (Figs. 6f and 7f). This suggests that the three parameters may play a different role on the charging and the charge separation inside the flow. For instance, since the total magnitude of discharges is proportional to both the total mass of the particles and the proportion of fine particles, the magnitude of the discharge is independent of the mass of larger particles, with the mass of fines being constant. However, experiments with few large particles will have more discharges (but smaller) than experiments with larger mass of big particles. Larger mass may generate larger turbulences, i.e. larger clusters of charges, and larger discharges. In this case, fewer discharges are necessary to discharge the total charge in the flow. Conversely, the total magnitude of the discharges is proportional to the mass of the fines which suggests that the key parameter is here the interaction between the fine and the large particles rather than the

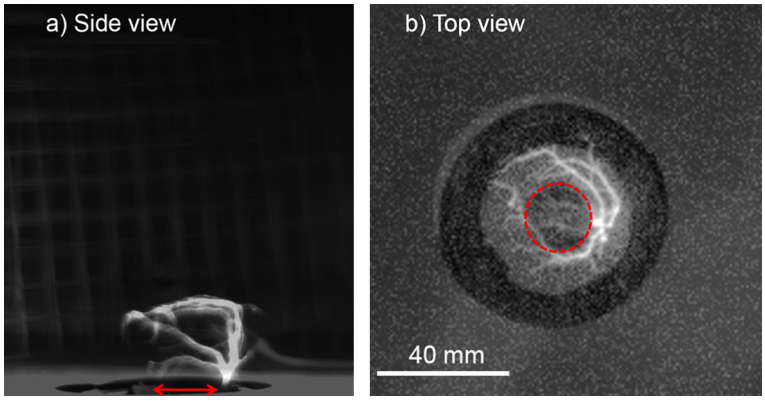

Fig. 8. Composite images of high-speed video still frames, showing the same flash seen from a) the side of the setup and b) the top orthogonal view of the setup. Red arrow and circles mark the location of the inner part of the autoclave (d_A in Fig. 2). The flash displays a main branch starting from the top of the nozzle and have some branches at the limit of the barrel shock structure (Mendez-Harper et al., 2018). In order to limit the effect of the particle jet obscuring the flash, the experiment was done in the dark, so that only the flash is visible. For spatial reference, still frames of the flash are superimposed to the pictures of the setup before the experimental run.

Table 1
Comparison of the main parameters and dimensionless numbers for our experiments and Sakurajima volcano (Japan). The maximum ash size in Sakurajima is computed as the maximum size that a particle can have so that its settling velocity as computed by the Stokes law is smaller than the buoyant rise velocity of the jet. Pressure at the vent is computed by scaling the pressure recorded at 3000 m (Cimarelli et al., 2016) to a 20 m vent diameter. Values for the dimensionless numbers correspond to the upper and lower bound of the values that can be obtained for the range of characteristic dimensions described in the upper part.

	Experiments	Sakurajima	Ratio Sakurajima/ Experiments
Main parameters			
Mass of ash [kg]	2.2×10^{-2}–5.99×10^{-2}	8×10^{6}–10^{8} [T]	10^{8}–10^{9}
Velocity [m/s]	200–500	100–300 [T]	0.5
Particle size [m]	10^{-6}–3×10^{-4}	10^{-6}–5×10^{-4} [T]	1
Temperature [k]	300	300–1000 [T]	1
Pressure at vent [Pa]	10^{5}–2×10^{6}	2×10^{5}–10^{7}	2–5
Vent diameter [m]	2.2×10^{-2}–3.7×10^{-2}	10–30	10^{3}
Gas viscosity [Pa s]	2.23×10^{-5}	1.85×10^{-5}–3.65×10^{-5}	1
Gas density [kg m^{-3}]	1–33	0.3–24	1
Time of last flash [s]	3×10^{-3}–7×10^{-3}	40–400 [C]	10^{4}–10^{5}
Jet dimensionless numbers			
Reynolds number	3×10^{5}–3×10^{7}	10^{7}–10^{10}	10^{2}
Stokes number	10^{-2}–10^{2}	10^{-4}–10^{4}	1
Froude number	3×10^{2}–10^{3}	5–3×10^{1}	10^{-2}
Electrical quantities			
Charge transfer per flash [C]	10^{-8}–10^{-7}	10^{-1} [A]	10^{6}–10^{7}
Number of recorded cloud to ground flashes	5–10	1–16 [C]	1
Cumulative magnitude of the discharges [C]	10^{-7}–10^{-6}	1	10^{6}–10^{7}

Data from [A] Aizawa et al. (2016); [C] Cimarelli et al. (2016); [T] Tournigand et al. (2017).

total surface area (which is not null in absence of small particles, unlike the total magnitude of the discharges).

4.2. Implications for volcanic processes

The shock tube apparatus has already demonstrated its capability to reproduce well the dynamics of volcanic jet flows (Alatorre-Ibargüengoitia et al., 2011; Cigala et al., 2017). Following the method by Cigala et al. (2017), we demonstrate (Table 1) that the flow conditions in our experiments realistically reproduce the conditions met at active volcanoes.

From a volcanic monitoring point of view, we demonstrate that vent discharges can be used not only as an early warning for ash-rich eruptions, but also potentially provide very accurate information about ash plume eruptions. For instance, since the total magnitude of the discharges is proportional at the same time to the mass of ash, the proportion of fines, and the initial pressure, we can summarize our experiments in a single plot linking the product of these three parameters with the electrical activity (Fig. 9). The low dispersion of the datapoints reflects the uncertainties of the methods and highlights the capabilities of the technique. These data are in good agreement with field observations clearly showing an increase of the electrical activity with the intensity and magnitude of the eruption, whether being the number of detected flashes (Arason et al., 2011; Cimarelli et al., 2016) or the presence and intensity of Continual Radio Frequency emissions (Behnke et al., 2018). From a quantitative point of view, the number of flashes produced is comparable to those observed at Sakurajima, but their magnitude is 10^{6}–10^{7} times lower (Table 1). This ratio can be compared to the mass ratio between Sakurajima and experiments (10^{8}–10^{9}), i.e. a discharge per mass unit which is 100 times larger in the experiments. That might be due to a different ash-size distribution with less fine particles in Sakurajima, or to less efficient differential charging mechanism: the maximum velocity is similar between our experiments and Sakurajima while the diameter differs by a factor 1000. Therefore, the velocity gradients must be much stronger in our experiment, leading to more efficient electrifications. However, the number of flashes is very similar, suggesting that the charge clusters have a comparable size, i.e. the charge separation mechanisms are similar.

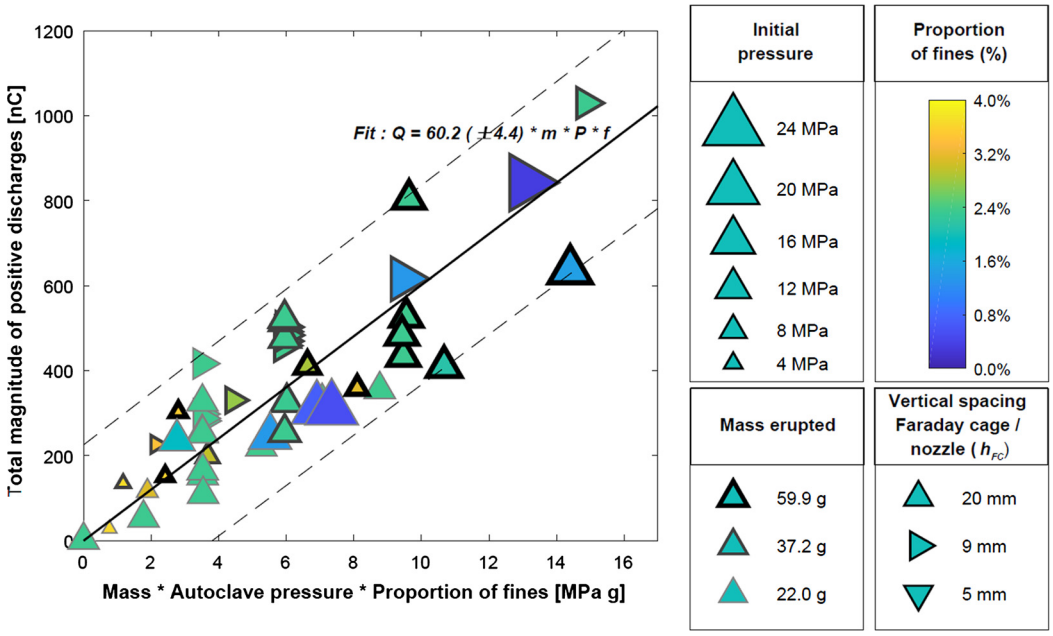

Fig. 9. Summary of all the experiments showing the relationship between the total magnitude of the positive discharge and the forcing parameters (initial pressure, proportion of fines and mass erupted). Note that the vertical spacing between the bottom of the Faraday cage and the nozzle rim (h_{FC}) induces a small, but noticeable variation, experiments with 20 mm spacing having a total magnitude of discharges decreased by ~20% compared to 5 mm.

Finally, we highlight that our experiments cannot catch the entire complexity of the volcanic electrification phenomenon. Concerning the electrification processes, a large difference between our experiments and the natural case is that we use fragmented samples as starting material. Tests using coherent samples did not display detectable lightning, probably because the experimental conditions are not sufficient to produce enough fine ash. As a consequence, we exclude particle electrification by fracto-emission from our analysis. Additionally, we deliberately excluded from the analysis some factors that may play a significant role on electrification, such as atmospheric conditions or ash characteristics (water content, composition, crystallinity or temperature). Another limitation of our experiment lies in the use of a metal (stainless-steal) autoclave, which might have very different tribological characteristics than the rocks forming a volcanic conduit. Finally, because of the small size of the autoclave, the ratio between vent diameter and particle diameter is higher than the natural case (Table 1), so a larger proportion of particles may be charged by the conduit wall than it might be in real volcanic conduits. These two last points will most likely impact the net charge of the flow (dashed lines in Fig. 4), but not the individual charge of large and fine particles responsible for the generation of the discharges.

5. Conclusions

In this paper, we present a first comprehensive methodology to compute the net charge of a volcanic plume within its jet phase as well as the number, magnitude and timing of vent discharges in the context of particle-laden jets produced in a shock-tube experimental setup. This new processing method allows the quantification of the effects of parameters which are relevant for volcanic eruptive columns (and other geophysical and industrial particle-laden flows) such as grainsize distribution, pressure at burst and mass of ejected particles on the electrical activity of the particle-laden jet. It will be also usable as a standard method for further studies to assess the effects of additional parameters such as ash composition, crystallinity and water content, or atmospheric conditions.

Our experiment highlights the occurrence of three phenomena determining the electrification pattern of the jet. First, the negative net charge of the particles in the flow is associated with the rubbing of the particles with the walls of the autoclave. The two key parameters are the mass, determining the amount of particle rubbing, and the energy of the explosion (corresponding to the pressure in our case) which sets the efficiency of the tribo-electrification. However, this phenomenon has no effect on the number or magnitude of discharges. The second phenomenon is the electrical charging within the jet. This depends on the energy of the jet, but also on the mass of fine particles, suggesting that particle–particle triboelectrification is the dominant mechanism with eventual contribution deriving from the disruption of electrostatic ash aggregates. The third phenomenon is the separation of the small negatively charged particles from the bigger positively charged ones, which is linked to the mass of big particles and the energy of the explosion. Both factors are key in determining the jet structure, and the size of the eddies associated with the turbulences.

The goal of the study is to represent the charging of volcanic ash plumes, and the associated cloud-to-ground vent discharges (note that the intracloud discharges do not change the total amount of charges within the Faraday cage; consequently, although being interesting for field studies they are not detectable in our experiments). Our results have important implications for the use of electric monitoring system at active explosive volcanoes, by showing that vent discharges can be used not only to detect in real time volcanic plume emissions, but, that also characterizing discharge properties such as length and magnitude might provide information on prevalent grain size and erupted mass in real time. Moreover, the variation of such parameters and the tempo of their occurrence during an eruption would give insights about the steadiness of the column and the pulsating behavior of the ash ejection (Dürig et al., 2015). The measured charges and discharges of our experiments cannot be directly extrapolated to the natural case in a quantitative way. However, they largely match with field observations on the direct relationship between explosion magnitude and the number and magnitude of discharges, highlighting

the future potential of this method for quantitative volcano monitoring.

Acknowledgements

This project has received funding from the European Union's Horizon 2020 research and innovation programme under the Marie Skłodowska-Curie Grant Agreement No. 705619. CC also acknowledges the support from National Geographic Society Exploration Grant No. GEFNE170-16 and the LMU Excellence Investment Fund. The authors thank B. Scheu, U. Kueppers, V. Cigala, the real J. Merisson and S. Alois for their help and support in designing the experiments, R. Ercoli, V. Becker, S. Stern and M. Knüver for their help in running the experiments and two anonymous reviewers and the editor Professor Tamsin Mather for their comments which greatly improved the manuscript.

References

Aizawa, K., Cimarelli, C., Alatorre-Ibarguengoitia, M.A., Yokoo, A., Dingwell, D.B., Iguchi, M., 2016. Physical properties of volcanic lightning: constraints from magnetotelluric and video observations at Sakurajima volcano, Japan. Earth Planet. Sci. Lett. 444, 45–55.

Alatorre-Ibargüengoitia, M.A., Scheu, B., Dingwell, D.B., 2011. Influence of the fragmentation process on the dynamics of Vulcanian eruptions: an experimental approach. Earth Planet. Sci. Lett. 302, 51–59.

Alatorre-Ibargüengoitia, M.A., Scheu, B., Dingwell, D.B., Delgado-Granados, H., Taddeucci, J., 2010. Energy consumption by magmatic fragmentation and pyroclast ejection during Vulcanian eruptions. Earth Planet. Sci. Lett. 291, 60–69.

Alidibirov, M., Dingwell, D.B., 1996. An experimental facility for the investigation of magma fragmentation by rapid decompression. Bull. Volcanol. 58, 411–416.

Alois, S., Merrison, J., Iversen, J.J., Sesterhenn, J., 2017. Contact electrification in aerosolized monodispersed silica microspheres quantified using laser based velocimetry. J. Aerosol Sci. 106, 1–10.

Arason, P., Bennett, A.J., Burgin, L.E., 2011. Charge mechanism of volcanic lightning revealed during the 2010 eruption of Eyjafjallajökull. J. Geophys. Res., Solid Earth 116, B00C03.

Behnke, S., Edens, H., Thomas, R., Smith, C., McNutt, S., Van Eaton, A., Cimarelli, C., Cigala, V., 2018. Investigating the origin of continual radio frequency impulses during explosive volcanic eruptions. J. Geophys. Res., Atmos. 123, 4157–4174.

Behnke, S.A., McNutt, S.R., 2014. Using lightning observations as a volcanic eruption monitoring tool. Bull. Volcanol. 76, 1–12.

Behnke, S.A., Thomas, R.J., McNutt, S.R., Schneider, D.J., Krehbiel, P.R., Rison, W., Edens, H.E., 2013. Observations of volcanic lightning during the 2009 eruption of Redoubt Volcano. J. Volcanol. Geotherm. Res. 259, 214–234.

Bennett, A., Odams, P., Edwards, D., Arason, Þ., 2010. Monitoring of lightning from the April–May 2010 Eyjafjallajökull volcanic eruption using a very low frequency lightning location network. Environ. Res. Lett. 5, 044013.

Cigala, V., Kueppers, U., Peña Fernández, J.J., Taddeucci, J., Sesterhenn, J., Dingwel, D.B., 2017. The dynamics of volcanic jets: temporal evolution of particles exit velocity from shock-tube experiments. J. Geophys. Res., Solid Earth 122, 6031–6045.

Cimarelli, C., Alatorre-Ibargüengoitia, M.A., Aizawa, K., Yokoo, A., Díaz-Marina, A., Iguchi, M., Dingwell, D.B., 2016. Multiparametric observation of volcanic lightning: Sakurajima Volcano, Japan. Geophys. Res. Lett., 4221–4228.

Cimarelli, C., Alatorre-Ibargüengoitia, M.A., Kueppers, U., Scheu, B., Dingwell, D.B., 2013. Experimental generation of volcanic lightning. Geology, G34802.34801.

Del Bello, E., Taddeucci, J., Scarlato, P., Giacalone, E., Cesaroni, C., 2015. Experimental investigation of the aggregation-disaggregation of colliding volcanic ash particles in turbulent, low-humidity suspensions. Geophys. Res. Lett. 42, 1068–1075.

Deng, H., He, Z., Xu, Y., Ma, J., Liu, J., Guo, R., 2010. An investigation on two-phase mixture discharges: the effects of macroparticle sizes. J. Phys. D, Appl. Phys. 43, 255203.

Douillet, G.A., Rasmussen, K.R., Kueppers, U., Castro, D.L., Merrison, J.P., Iversen, J.J., Dingwell, D.B., 2014. Saltation threshold for pyroclasts at various bedslopes: wind tunnel measurements. J. Volcanol. Geotherm. Res. 278, 14–24.

Dürig, T., Gudmundsson, M.T., Karmann, S., Zimanowski, B., Dellino, P., Rietze, M., Büttner, R., 2015. Mass eruption rates in pulsating eruptions estimated from video analysis of the gas thrust-buoyancy transition—a case study of the 2010 eruption of Eyjafjallajökull, Iceland. Earth Planets Space 67 (1), 180.

Ergun, S., 1952. Fluid flow through packed columns. Chem. Eng. Prog. 48, 89–94.

Forward, K.M., Lacks, D.J., Sankaran, R.M., 2009. Charge segregation depends on particle size in triboelectrically charged granular materials. Phys. Rev. Lett. 102, 028001.

Gaudin, D., Cimarelli, C., 2019. Experimental dataset of charges and discharges measurement during shock-tube experiments. V. 1.0. GFZ Data Services. https://doi.org/10.5880/fidgeo.2018.025.

Harrison, R.G., Nicoll, K., Ulanowski, Z., Mather, T., 2010. Self-charging of the Eyjafjallajökull volcanic ash plume. Environ. Res. Lett. 5, 024004.

Houghton, I.M., Aplin, K.L., Nicoll, K.A., 2013. Triboelectric charging of volcanic ash from the 2011 Grímsvötn eruption. Phys. Rev. Lett. 111, 118501.

James, M.R., Lane, S.J., Gilbert, J.S., 2000. Volcanic plume electrification: experimental investigation of a fracture-charging mechanism. J. Geophys. Res., Solid Earth 105, 16641–16649.

James, M.R., Lane, S.J., Gilbert, J.S., 2003. Density, construction, and drag coefficient of electrostatic volcanic ash aggregates. J. Geophys. Res., Solid Earth 108.

James, M.R., Wilson, L., Lane, S.J., Gilbert, J.S., Mather, T.A., Harrison, R.G., Martin, R.S., 2008. Electrical charging of volcanic plumes. In: Leblanc, F., Aplin, K.L., Yair, Y., Harrison, R.G., Lebreton, J.P., Blanc, M. (Eds.), Planetary Atmospheric Electricity. Springer, New York, pp. 399–418.

Kueppers, U., Scheu, B., Spieler, O., Dingwell, D.B., 2006. Fragmentation efficiency of explosive volcanic eruptions: a study of experimentally generated pyroclasts. J. Volcanol. Geotherm. Res. 153, 125–135.

Lacks, D.J., Levandovsky, A., 2007. Effect of particle size distribution on the polarity of triboelectric charging in granular insulator systems. J. Electrost. 65, 107–112.

Lee, V., Waitukaitis, S.R., Miskin, M.Z., Jaeger, H.M., 2015. Direct observation of particle interactions and clustering in charged granular streams. Nat. Phys. 11, 733.

McNutt, S.R., Williams, E.R., 2010. Volcanic lightning: global observations and constraints on source mechanisms. Bull. Volcanol. 72, 1153–1167.

Méndez Harper, J., Dufek, J., 2016. The effects of dynamics on the triboelectrification of volcanic ash. J. Geophys. Res., Atmos. 121, 8209–8228.

Méndez Harper, J., Dufek, J., McAdams, J., 2015. The electrification of volcanic particles during the brittle fragmentation of the magma column. In: Proc. ESA Annual Meeting on Electrostatics, p. 10.

Méndez Harper, J.S., Cimarelli, C., Dufek, J., Gaudin, D., Thomas, R., 2018. Inferring compressible fluid dynamics from vent discharges during volcanic eruptions. Geophys. Res. Lett.

Miura, T., Koyaguchi, T., Tanaka, Y., 2002. Measurements of electric charge distribution in volcanic plumes at Sakurajima Volcano, Japan. Bull. Volcanol. 64, 75–93.

Mueller, S.B., Ayris, P.M., Wadsworth, F.B., Kueppers, U., Casas, A.S., Delmelle, P., Taddeucci, J., Jacob, M., Dingwell, D.B., 2017. Ash aggregation enhanced by deposition and redistribution of salt on the surface of volcanic ash in eruption plumes. Sci. Rep. 7, 45762.

Surplice, N.A., D'Arcy, R.J., 1972. Reduction in the work function of stainless steel by electric fields. J. Phys. F, Met. Phys. 2 (1), L8–L10. https://doi.org/10.1088/0305-4608/2/1/003.

Thirumal Murugan, J., Suresh Kumar, T.R., Salil, P., Venkatesh, C., 2015. Dual frequency selective transparent front doors for microwave oven with different opening areas. PIER Lett. 52, 11–16. https://doi.org/10.2528/pierl14121801.

Thomas, R.J., Krehbiel, P.R., Rison, W., Edens, H., Aulich, G., Winn, W., McNutt, S.R., Tytgat, G., Clark, E., 2007. Electrical activity during the 2006 Mount St. Augustine volcanic eruptions. Science 315, 1097.

Thomas, R.J., Krehbiel, P.R., Rison, W., Hunyady, S.J., Winn, W.P., Hamlin, T., Harlin, J., 2004. Accuracy of the lightning mapping array. J. Geophys. Res., Atmos. 109.

Thomas, R.J., McNutt, S.R., Krehbiel, P.R., Rison, W., Aulich, G., Edens, H., Tytgat, G., Clark, E., 2010. Lightning and Electrical Activity During the 2006 Eruption of Augustine Volcano. US Geological Survey.

Tournigand, P.Y., Taddeucci, J., Gaudin, D., Peña Fernández, J.J., Del Bello, E., Scarlato, P., Kueppers, U., Sesterhenn, J., Yokoo, A., 2017. The initial development of transient volcanic plumes as a function of source conditions. J. Geophys. Res., Solid Earth.

Van Eaton, A., Schneider, D., Cervelli, P., Holzworth, R.H., Lyons, J., Haney, M., Wallace, K., Fee, D., Mastin, L.G., 2017. Volcanic lightning during the shallow submarine eruption of Bogoslof volcano, Alaska. In: IAVCEI 2017 Scientific Assembly, Portland, USA.

Van Eaton, A.R., Amigo, Á., Bertin, D., Mastin, L.G., Giacosa, R.E., González, J., Valderrama, O., Fontijn, K., Behnke, S.A., 2016. Volcanic lightning and plume behavior reveal evolving hazards during the April 2015 eruption of Calbuco volcano, Chile. Geophys. Res. Lett. 43, 3563–3571.

Wilson, R.G., 1966. Vacuum thermionic work functions of polycrystalline Be, Ti, Cr, Fe, Ni, Cu, Pt, and type 304 stainless steel. J. Appl. Phys. 37 (6), 2261–2267. https://doi.org/10.1063/1.1708797.

Wörner, G., Schmincke, H.-U., 1984. Mineralogical and chemical zonation of the Laacher See tephra sequence (East Eifel, W. Germany). J. Petrol. 25, 805–835.